VCSEL-pumped Nd:YAG laser with 95 W average power and user-selectable nanosecond pulses

Chao Wang (汪 超)[1,2,*], Hui Wei (韦 辉)[1,], Youen Jiang (姜有恩)[1], Jiangfeng Wang (王江峰)[1], Zhi Qiao (乔 治)[1,2], Jiangtao Guo (郭江涛)[1,2], Wei Fan (范 薇)[1], and Xuechun Li (李学春)[1]**

[1]*Shanghai Institute of Optics and Fine Mechanics, Chinese Academy of Sciences, Shanghai 201800, China*
[2]*University of Chinese Academy of Science, Beijing 100049, China*
**Corresponding author: wangchao@siom.ac.cn; **corresponding author: weihuicn@hotmail.com*
Received August 22, 2016; accepted October 28, 2016; posted online November 30, 2016

A 95 W Nd:YAG laser system pumped by a vertical cavity surface emitting laser (VCSEL) array is described. The laser contains an all-fiber-based seeder, an Nd:YAG regenerative amplifier, and a four-pass amplifier. The laser operates at 300 Hz with energies up to 317 mJ. The beam has a top-hat intensity distribution. The temporal pulse shape is flat in time, and the pulse width can be adjusted in the range of 2–6 ns.

OCIS codes: 140.3280, 140.3295, 140.6810, 140.7260.
doi: 10.3788/COL201614.121402.

Inertial confinement fusion (ICF) laser drivers are designed to deliver pulses with several million joules within several nanoseconds. Therefore, optics should withstand extremely intense laser pulses. Optics damage induced by very-high-peak power is one of the factors that add to the experiment cost and decrease operation efficiency[1]. Laser-induced optics damage is related to the laser wavelength, laser fluence, pulse width, and pulse shape[2–5]. A high-peak-power (HPP), high-average-power (HAP) laser system that has a flat-in-time (FIT) pulse shape with an adjustable pulse width (within several nanoseconds) as well as a spatially flat beam profile, can be a powerful tool for studying optics damage for ICF laser drivers.

A master oscillator power amplifier (MOPA) is an effective way to achieve HPP and HAP laser operation as well as a good beam quality. The oscillator can be a quality-switched (Q-switched) laser or a mode-locked laser[6–11]. However, neither of the two lasers can generate a seed with an FIT pulse shape. The front-end in the ICF laser is an excellent source to generate such a seed[12,13]. Lamp-pumped high-energy Nd:YAG rod laser systems are usually limited to operating with a repetition rate of 10 Hz, owing to the severe thermal load, the beam quality degradation, and the lamp durability. Diode-pumping is an effective way to mitigate the thermal effects, increase the operation repetition rate, and improve the average power.

Previously, a diode-pumped Nd:YAG system that could deliver 112 mJ pulses at 100 Hz was reported by our team[14]. The average power is limited by severe thermal effects, crystal fractures, and parasitic oscillation. Vertical cavity surface emitting laser (VCSEL) arrays have developed rapidly in recent years[15,16]. In solid state lasers, VCSEL is an attractive pumping source due to the combined advantages of low cost, high reliability, a narrow and thermally stable spectrum, high-power scalability, easy system integration, etc. In this Letter, we report our results on a refined VCSEL-pumped Nd:YAG laser system that delivers 317 mJ pulses at a wavelength of 1064 nm and a repetition rate of 300 Hz. The average power reaches up to 95 W, and the spatial profile of the beam is near top-hat intensity. The pulse shape is FIT, and the pulse width is selectable from 2 to 6 ns. The laser system contains three parts: an all-fiber-based seeder, an Nd:YAG regenerative amplifier, and a four-pass Nd:YAG amplifier, with both amplifiers pumped by VCSELs. The laser amplifier system is in an 80 cm by 200 cm breadboard.

Figure 1 shows the major functions of the all-fiber-based seeder in the block diagram. The oscillator is a single-mode distributed-feedback (DFB) fiber laser, which generates the initial continuous wave (CW) light. The CW light is chopped into 200 ns pulses at 300 Hz by an acousto-optic (AO) modulator. The output of the AO is amplified by a fiber amplifier and modulated by an electro-optic waveguide amplitude modulator. The pulse shape and the pulse width can be adjusted by changing the electronic signal applied to the amplitude modulator. Lastly, the pulses from the amplitude modulator are amplified by the second fiber amplifier, and the pulse energy reaches 1 nJ. The electronic signal is generated by a square pulse generator (SPG) in the current system. In the experiment, the seed pulse width can be adjusted in the range of 2–10 ns.

The setup of the regenerative amplifier and the four-pass amplifier is shown in Fig. 2. The seed laser from the fiber is collimated by an aspheric lens (L1), and then injected into the regenerative amplifier. The cavity of the

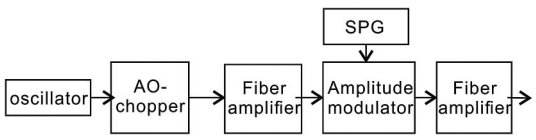

Fig. 1. Functional block diagram of the seeder.

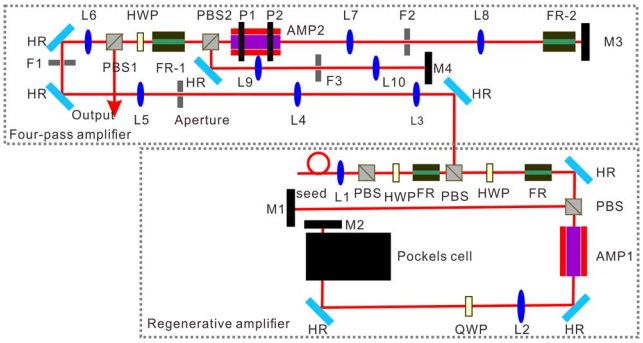

Fig. 2. Schematic of the regenerative amplifier and the four-pass amplifier, which includes Nd:YAG laser heads (AMP1 & AMP2), mirrors (M1–M4), 45° reflectors (HR), lenses (L1–L10), polarization beam splitter (PBS), Faraday rotators (FR), half wavelength plates (HWP), beam focuses (F1~3), the first principal plane of the rod (P1), and the second principal plane of the rod (P2).

regenerative amplifier has a length of 4 m. The laser head (AMP1) is in the middle of the cavity. The gain medium is a $\varnothing 4 \times 80$ mm, 0.8% Nd:YAG rod, which is quasi-continuously pumped by nine VCSEL chips of 100 W at 300 Hz with a pulse width of 270 μs. The Pockels cell is switched on for a duration of ~1000 ns, and the pulse travels ~40 round trips in the cavity. The pulse energy after the regenerative amplifier reaches 3 mJ.

The coaxial four-pass amplifier is designed to meet the image relaying relation for a good beam quality. The heated Nd:YAG rod can be treated as a thick lens with two principal planes (P1, P2). Before being injected into the four-pass cavity, the beam from the regenerative amplifier is expanded by a telescope (L3 $f = -100$ mm, L4 $f = 500$ mm), and the expanded beam passes through an 8.5 mm aperture. The aperture as the original object plane is relay-imaged onto P1 by L5 and L6. After the first-pass amplification, the beam exits the module from P2. P2 is relay-imaged onto mirror M3 by L7 and L8. Then, the beam is reflected by M3, and the second-pass amplification occurs. The beam polarization rotates 90° after two passes through Faraday rotator FR-2. After exiting the module from P1, the beam is reflected by polarization beam splitter PBS2, and relay-imaged onto M4 by L9 and L10. Then, the beam is reflected by M4, and the third- and fourth-pass amplification follows. Finally, the beam polarization rotates another 90° after another two passes through FR-2, and the beam transmits from PBS2. The pulse energy reaches 317 mJ after the four-pass amplifier.

Three 4F imaging optical systems (L5 and L6, L7 and L8, and L9 and L10) are used to maintain the image relaying relation in the four-pass amplifier. There are three focuses (F1, F2, and F3) in these imaging optical systems. In this setup, the energy density at F1 and F2 is relatively low, and there is no risk of air-breakdown. The pulse energy reaches ~100 mJ at F2 after three passes through the laser head; hence, a vacuum tube is placed between L7 and L8 to avoid air-breakdown.

Severe thermal effects of the gain medium in the four-pass amplifier make it very challenging to develop such a laser system. The laser head used in the four-pass amplifier is the key element for achieving a good beam quality. Figure 3 shows the pumping configuration of the module. The module has a $\varnothing 9 \times 120$ mm, 0.6% Nd:YAG rod. The VCSEL chip from the new diode laser (NDL) has a size of 4.7 mm × 4.7 mm, and the beam divergence is 250 μrad × 250 μrad. The electro-optic efficiency of the VCSEL chip is 40%. Seven rows of 11 VCSEL chips are placed around the rod, and an Au-coated reflective chamber is used to improve the pumping efficiency. The outer surface of the glass tube is roughened to improve the pumping uniformity. The operating voltage of the module is 218 V, and the module is operated at 115 A for 230 μs for each pulse, which matches the upper state lifetime of the gain medium. The liquid channels for the rod and the heat sink of the VCSEL chips are connected in series for effective cooling. The beam from the regenerative amplifier is expanded as a probe light to measure the gain distribution over the cross section of the rod. The gain distribution is shown in Fig. 4. The gain profile is flat in the center of the rod, but the gain at the edge of the rod is higher than the one in the center. This leads to a nonuniform amplification. A gauss-profile beam is injected into the amplifier to pre-compensate for the inhomogeneity of the gain distribution[17].

The combination of volumetric heating of the cylindrical rod by the pumping and surface cooling required for the heat extraction leads to a nonuniform temperature distribution over the cross section of the rod. This results in a wavefront distortion of the laser beam. The thermal effects contain thermal lensing and stress-induced

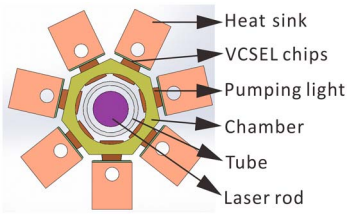

Fig. 3. Pumping configuration of the module used in the four-pass amplifier.

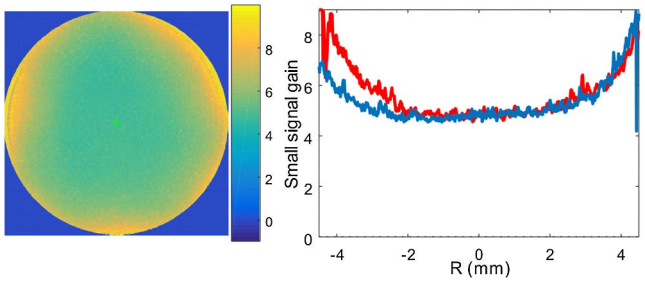

Fig. 4. Gain distribution over the cross section of the rod; the red line and the blue line represent the gain distribution along the horizontal and vertical center line of the cross section of the rod.

birefringence. The stress-induced birefringence in the rod leads to depolarization. This results in parasitic oscillation in the four-pass amplifier as well as a large cavity loss. The principal axes of the stress-induced birefringence are radially and tangentially directed at each point in the cross section of the rod[18]. The compensation scheme shown in Fig. 5 is refined from that used in Ref. [19]. The basic idea of the compensation is the simultaneous use of an in-cavity polarization rotator (FR-2) and an imaging optical system (L7, L8) between the two passes through the laser rod. The beam travels the same path through the rod twice with a 90° polarization rotation in between. Therefore, the optical length of the radial and tangential polarization is equal, and the stress-induced birefringence can be compensated for. The distance between L7 and L8 is finely adjusted to compensate for the thermal lensing. Here, $d = 2f - (f_r + f_\varphi)f^2/2f_r f_\varphi$, where f_r and f_φ represent the focal length of the rod for radially and tangentially polarized radiation, respectively.

Parasitic oscillation is another challenge in the four-pass amplifier. The cavity transmission per pass (T_1) is 0.9. The maximum small signal gain factor per pass (G_0) is ~8 at the rod edge, owing to the inhomogeneity of the gain distribution. Three factors can lead to parasitic oscillation. The first one is the finite extinction ratio of PBS2 and FR-2. Both the PBS and FR have an extinction ratio (P_e) of 1000:1; the gain factor caused by it is $G_0^2 T_1^2 P_e = 0.06$, which is not of any concern. The second one is the depolarization of the beam in the laser rod, owing to the incomplete compensation of the stress-induced birefringence. The depolarization loss (P_d) is measured in the double-pass scheme by comparing the pulse energy at M4 (E_1) to that after PBS1 (E_2). The measured P_d after the compensation is 0.4%. Thus, the maximum gain factor is $G_0^2 T_1^2 P_d = 0.24$; it will not oscillate. The third one is the weak reflections from the anti-reflective (AR) coatings ($R_{\text{glint}} < 0.5\%$ for standard AR coatings). In four-pass amplifiers, weak glints from optical surfaces at different positions have different gains. It is the optical surfaces between PBS2 and AMP2 whose glints lead to the highest gain[20]. The maximum gain factor is $G_0^4 T_1^4 R_{\text{glint}} = 16$. Therefore, the system will easily oscillate. To suppress glint-induced parasitic oscillation, the optics with AR coatings are all tilted, and a 2 mm aperture is placed at F2 to block the glints. The number of optics between PBS2 and AMP2 is minimized to further reduce the risk of parasitic oscillation. Therefore, PBS2 is placed near AMP2 rather than M4. No parasitic oscillation is observed in the experiment with these measures.

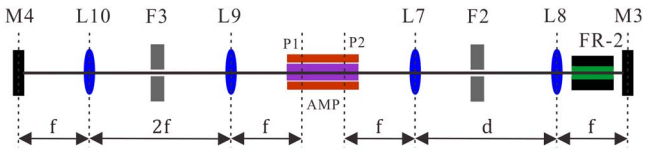

Fig. 5. Principle of the birefringence compensation.

The relation between the output and the input pulse energy of the four-pass amplifier can be seen in Fig. 6. The output energy reaches 317 mJ with the maximum injected pulse energy. The optical-to-optical efficiency is 13.4% (the laser power versus the pumping light power). The beam profile that is measured with an imaging setup after PBS1 is shown in Fig. 7, where the output energy is 317 mJ, and the pulse width is 4 ns. The binary beam image file has a one-to-one correspondence between the relative fluence per pixel and the pixel value. The pixels, whose value exceeds 10% of the maximum value, are defined as the region of interest (ROI). The intensity modulation is defined as the ratio of the maximum pixel value to the average pixel value within the ROI. A top-hat beam profile is obtained on the image plane with an intensity modulation of 1.8. To further describe the beam profile, a histogram of all of the pixels within the ROI is generated. The 10% energy fraction is defined as the ratio of the number of pixels whose pixel value falls within −5% of the mean pixel value to the number of pixels within the ROI[21]. The 20% energy fraction and the 40% energy fraction are defined in the same way.

The output energy of the four-pass amplifier is limited by the output of the regenerative amplifier and the beam profile. A top-hat beam profile is obtained when the pulse energy reaches 317 mJ. Because of the saturation, further increasing the output energy will lead to a V-shaped beam profile similar to the gain distribution in Fig. 4.

The output beam wavefront is obtained by a wavefront sensor (SID4 from Phasics) that shown in Fig. 8. The peak-to-valley value of the wavefront is 2.03 λ, and the root mean square is 0.3 λ. Because of the pumping inhomogeneity, the heat generated in the gain medium is

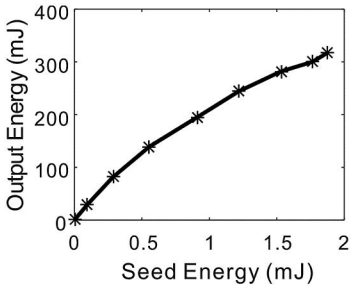

Fig. 6. Output energy versus input energy of the four-pass amplifier.

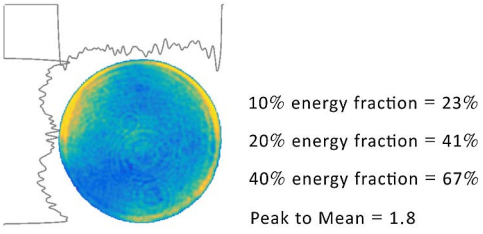

Fig. 7. Output beam profile measured on the image plane.

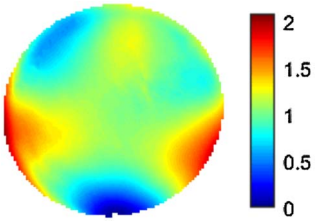

Fig. 8. Wavefront distribution measured on the image plane.

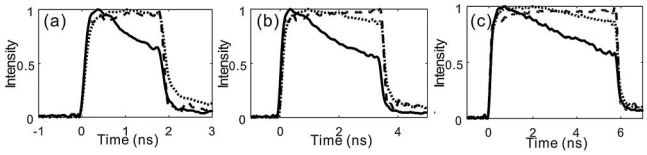

Fig. 9. Temporal profiles for (a) 2, (b) 4, and (c) 6 ns pulses, respectively. The dashed line, the dotted line, and the solid line represent the pulse shape of the seed, the regenerative amplifier, and the four-pass amplifier, respectively.

nonuniform. This leads to a temperature distribution deviating from the parabolic profile, as well as the thermally induced wavefront distortion. The beam quality degrades dramatically after four passes. A better beam quality can be expected by refining the pumping profile.

The pulse shape is obtained by using a 15 G high-speed photoelectric detector (ET-3500) and an oscilloscope (Tektronix 70404C) with a sampling rate of 25 GS/s. The temporal profiles of the pulse for 2, 4, and 6 ns are shown in Fig. 9, and the square pulse distortion (SPD) is ~1.7. The pulse shapes for different pulse widths are nominally FIT. The SPD can be pre-compensated for by the all-fiber-based seeder. The pulse width is limited to 6 ns to avoid the pulse overlap in the gain medium.

In conclusion, we demonstrate a 95 W Nd:YAG laser system based on an MOPA. The MOPA includes a 1 nJ all-fiber-based seeder, a 3 mJ regenerative amplifier, and a four-pass amplifier. The VCSEL-pumped laser head used in the four-pass amplifier is developed. The thermally induced birefringence and the pumping inhomogeneity are compensated for, and parasitic oscillation is suppressed in the four-pass amplifier. The laser operates at 300 Hz with pulse energies of up to 317 mJ. The beam has a top-hat profile in the near field, and the pulse shape is FIT. The pulse width is user selectable in the range of 2–6 ns. With these characteristics, the laser system can be an effective tool to study optics damage. In the next step, we will optimize the output beam quality and begin frequency conversion experiments to further the applications of this laser system. The SPG will be replaced by an arbitrary waveform generator in the all-fiber-based seeder to pre-compensate for the SPD and add the capability of adjusting the pulse shape.

References

1. M. L. Spaeth, K. R. Manes, D. H. Kalantar, and P. E. Miller, Fusion Sci. Technol. **69**, 25 (2016).
2. E. S. Bliss, Opto-Electron. **3**, 99 (1971).
3. K. Starke, T. Grob, D. Ristau, W. Riggers, and J. Ebert, Proc. SPIE **3578**, 584 (1998).
4. B. C. Stuart, M. D. Feit, A. M. Rubenchik, B. W. Shore, and M. D. Perry, Phys. Rev. Lett. **74**, 2248 (1995).
5. C. W. Carr, J. B. Trenholme, and M. L. Spaeth, Appl. Phys. Lett. **90**, 041110 (2007).
6. C. Baumgarten, M. Pedicone, H. Bravo, H. Wang, L. Yin, C. S. Menoni, J. J. Rocca, and B. A. Reagan, Opt. Lett. **41**, 3339 (2016).
7. J. S. Qin, X. X. Tang, Z. W. Fan, and H. C. Wang, Opt. Commun. **368**, 68 (2016).
8. D. W. E. Noom, S. Witte, J. Morgenweg, R. K. Altmann, and K. S. E. Eikema, Opt. Lett. **38**, 3021 (2013).
9. B. Liu, Z. Wang, F. Yang, Z. Wang, Y. Bo, H. Yuan, L. Yuan, B. Wang, J. Xu, Y. Guo, Q. Peng, J. Zhang, D. Cui, and Z. Xu, Chin. Opt. Lett. **12**, 031404 (2014).
10. Q. Yang, X. Zhu, J. Ma, T. Lu, X. Ma, and W. Chen, Chin. Opt. Lett. **13**, 061401 (2015).
11. H. Yang, J. Meng, X. Ma, and W. Chen, Chin. Opt. Lett. **12**, 121406 (2014).
12. M. D. Skeldon, J. Opt. Soc. Am. B **19**, 2423 (2002).
13. P. J. Wisoff, M. W. Bowers, G. V. Erbert, D. F. Browning, and D. R. Jedlovec, Proc. SPIE **5341**, 146 (2004).
14. C. Wang, H. Wei, J. F. Wang, E. Y. Jiang, W. Fan, and C. X. Li, Acta. Phys. Sin. **63**, 22 (2014).
15. J. F. Seurin, G. Y. Xu, V. Khalfin, A. Miglo, J. D. Wynn, P. Pradhan, C. L. Ghosh, and L. A. D. Asaro, Proc. SPIE **7229**, 3 (2009).
16. R. V. Leeuwen, T. Chen, L. Watkins, G. Y. Xu, J. F. Seurin, Q. Wang, D. L. Zhou, and C. Ghosh, Proc. SPIE **9342**, 20 (2015).
17. T. Z. Zhao, H. Xiao, K. Huang, and Z. W. Fan, Proc. SPIE **9673**, 3 (2015).
18. W. Koechner, *Solid-State Laser Engineering* (Springer-Verlag, 2006).
19. Q. Lu, N. Kugler, H. Weber, S. Dong, N. Muller, and U. Wittrock, Opt. Quantum Electron. **28**, 57 (1996).
20. B. D. Moran, C. B. Dane, J. Crane, M. Martinez, F. Penko, and L. Hackel, Proc. SPIE **3264**, 56 (1998).
21. J. Honig, J. Halpin, D. Browning, J. Crane, R. Hachel, M. Henesian, J. Peterson, D. Ravizza, T. Wennberg, H. Rieger, and J. Marciante, Appl. Opt. **46**, 3269 (2007).